Detection of Foreign Bodies and Bubble Defects in Tire Radiography Images Based on Total Variation and Edge Detection *

ZHANG Yan(张岩), LI Tao(李涛), LI Qing-Ling(李庆领)**

College of Electromechanical Engineering, Qingdao University of Science and Technology, Qingdao 266061

We present the analysis and decomposition of tire radiography images by combining the total variation, curvelet transform based image enhancement, and Canny edge detection to detect foreign bodies and bubble defects in tires. Relying on the feature of total variation that images can be decomposed as texture parts and cartoon parts, we decompose the tire radiography image and select the cartoon part for defect detection since the textures are segmented and defect information is retained. The edges of the image are enhanced by modifying the curvelet coefficients before further edge detection operation. Furthermore, a Canny edge detection operator is used to detect the defects in which the eight-neighborhood bilinear interpolation non-maximum suppression method is employed to improve the detection performance. In our experiments, the Sobel operator and state-of-the-art methods such as the LoG operator and Canny edge detection algorithms are employed for comparison, and the experimental results are discussed briefly. The experimental results indicate that foreign bodies and bubbles in tires can be detected and located accurately by our proposed method.

Tire defects, adverse road conditions, or a combination of the two play a key role in road accidents.[1,2] Tire inspection has already become an important issue for researchers and tire manufacturers in order to improve safety. For this purpose, non-destructive testing (NDT) techniques have been employed to test a material for surface or internal flaws without interfering in any way with its suitability for service.[3] The most commonly used methods include acoustic emission, magnetic particle inspection, eddy current, ultrasonic testing, thermal inspection, and several others.[4,5] The overall effects available for these techniques are either quite limited or appropriate only for a specific type of defect. Radioscopy, especially x-ray, on the other hand, is one of the most effective tools for tire defect detection, and has been widely used in manufacturing processes. Radiography images are based on the transmission of quanta through the object, with contrast occurring due to variations in thickness and composition.

Radiography (x-rays or sometimes gamma rays) seems to be the most effective method due to its advantages that both surface and internal discontinuities can be detected, significant variations in composition can be detected, there are very few material limitations, and a permanent test record is obtained. Researchers employ image processing and pattern recognition methods to give objective, reliable and consistent results automatically in the inspection process.[4−8]

Radiography image-based defect detection technology has been widely used in industrial applications such as fabric defect detection and weld defect detection, etc. A comparison study of weld defect segmentation is assessed in Ref. [9]. Sofia and Redouane described a defect segmentation method based on a watershed algorithm and morphological operations.[10] Carrasco and Mery proposed a set of image processing techniques such as a bottom hat filter that was combined to segment defects.[11]

However, it is difficult to define the features of tire radiography images due to their multi-textural characteristics. The inconsistency of the textures in different sections of tire radiography images is another obstacle for feature selection. Moreover, various defect types make the detection and segmentation of defects more difficult. By virtue of the total variation feature, in which images can be decomposed as texture parts and cartoon parts, in this work we utilize the total variation-based cartoon and texture decomposition algorithm[12] to decompose the tire radiography image $f(x, y)$ into the sum of a cartoon part, u, where only the image contrasted shapes appear, and a textural part, v, with oscillating patterns. The foreign bodies and bubble defects of the tire radiography images are included in the u part, and therefore the textural part will not affect the defect detection process thereafter. In the curvelet domain, the edge features can be represented with the larger coefficients in the sub-highest frequency band. Based on this feature, we enhance the image edges by modifying the curvelet coefficients before further edge detection operations. We detect defects in the cartoon part using edge detection. An eight-neighborhood bilin-

ear interpolation non-maximum suppression method, which outperforms the eight-neighborhood gradient value method, is introduced to increase edge detection accuracy.

Total variation is widely used in digital image processing, especially in denoising known as total variation regularization. The main characteristics of a textured region are its high total variation. Let $f : R^2 \rightarrow R$ be a given image. In real applications, the observed image f is just a noisy version of a true image u. It is a textured image, and u would be a simple sketchy approximation or a cartoon image of $f(x,y)$. In the presence of additive noise, the relation between u and $f(x,y)$ can be expressed by the linear model, introducing another function v, and such that $f(x,y) = u(x,y) + v(x,y)$.[13]

The formalization of this remark leads to the definition of local total variation (LTV) for every pixel (x,y),

$$\text{LTV}_\sigma(x,y)(f) := G_\sigma * |\nabla f|(x,y), \tag{1}$$

where G_σ is a Gaussian kernel with standard deviation σ; $|\nabla f|$ is the gradient mode of $f(x,y)$; and $*$ represents the convolution. The relative reduction rate of LTV is defined as

$$\lambda(x,y) := \frac{\text{LTV}_\sigma(x,y)(f) - \text{LTV}_\sigma(x,y)(L_\sigma * f)}{\text{LTV}_\sigma(x,y)(f)}, \tag{2}$$

where L_σ a low pass filter. As LTV decreases very quickly under low pass filtering, $\lambda(x,y)$ gives us the local oscillatory behavior of the function.

$$\frac{\text{LTV}_\sigma(f) - \text{LTV}_\sigma(L_\sigma * f)}{\text{LTV}_\sigma(f)} = \lambda$$
$$\Leftrightarrow \text{LTV}_\sigma(L_\sigma * f) = (1 - \lambda)\text{LTV}_\sigma(f). \tag{3}$$

If λ is close to 0, there is little relative reduction in the local total variation by the low pass filter. If instead λ is close to 1, then the reduction will be strong, which means that the considered point belongs to a textured region. Thus, a fast nonlinear low pass and high pass filter pair can be computed by performing weighted averages of $f(x,y)$ and $L_\sigma * f$ depending on the relative reduction in LTV,

$$u(x,y) = w(\lambda(x,y))L_\sigma * f + (1 - w(\lambda(x,y)))f, \tag{4}$$

$$v(x,y) = f(x,y) - u(x,y), \tag{5}$$

where $w(x,y):[0,1] \rightarrow [0,1]$ is a non-decreasing piecewise affine function that is constant and equal to zero near zero, and is constant and equal to 1 near 1.

In all experiments, the soft threshold parameters defining w have been fixed to $a_1 = 0.25$ and $a_2 = 0.5$. If $\lambda(x,y)$ is small, the function $f(x,y)$ will be non-oscillatory around (x,y) and therefore the function

will be BV around (x,y). Thus $u(x,y) = f(x,y)$ is the right choice. If instead λ is large, then the function f is locally oscillatory and locally replaced by $L_\sigma * f$.

The choice of $\lambda = 1/2$ as the underlying hard threshold is conservative: it ensures that all step edges stay on the cartoon side, but it puts all fine structures on the texture side as soon as they oscillate more than once. Since it is desirable to have a one-parameter method, λ is fixed once and for all. In this way, the method retains the scale of the texture as the only method parameter. The scale parameter is measured in pixel size, and thus $\sigma = 2$ roughly means that the texture half-period is 2 pixels. With $\sigma = 2$, only the finest textures are distinguished. In general, researchers perceive image regions as textures for values ranging from $\sigma = 3$ to 6. Over this last value, the textures are made of well distinguished and contrasted objects, and the decision to view them as a texture is definitely subjective. Figure 1 shows an experimental result of the Barbara test image with $\sigma = 3.0$.

Fig. 1. Experimental result of the Barbara test image with $\sigma = 3.0$. (a) The Barbara test image, (b) the texture part of Barbara, and (c) the cartoon part of Barbara. The texture image is obtained as the difference between the original and cartoon images. The range in differences, $[-20, 20]$, is linearly transformed to $[0, 255]$ for visualization purposes. Differences outside this range are saturated to 0 and 255, respectively.

There are many edge detection methods, which can be grouped into two categories, search-based and zero-crossing-based. Although Canny's work was carried out in the early days of computer vision, the Canny edge detector (including its variations) is still a state-of-the-art edge detector.[14] The Canny edge detector uses a filter based on the first derivative of a Gaussian, because it is susceptible to noise presenting on raw unprocessed image data, so to begin with, the raw image is convolved with a Gaussian filter.

$$M(x,y) = G(x,y,\sigma) \cdot f(x,y), \tag{6}$$

where $f(x,y)$ is the original image, and $G(x,y,\sigma)$ is the Gaussian smoothing operator. An edge in an image may point in a variety of directions, so the Canny algorithm uses four filters to detect horizontal, vertical and diagonal edges in the blurred image when finding the intensity gradient of the image.

$$S(x,y) = \sqrt{P^2(x,y) + Q^2(x,y)}, \tag{7}$$

$$\theta(x,y) = \arctan|Q(x,y)/P(x,y)|, \tag{8}$$

where

$$P(x,y) \approx \frac{1}{2}[M(x,y+1) - M(x,y) + M(x+1,y+1)$$
$$- M(x+1,y)], \qquad (9)$$

$$Q(x,y) \approx \frac{1}{2}[M(x,y) - M(x+1,y) + M(x,y+1)$$
$$- M(x+1,y+1)]. \qquad (10)$$

Given estimates of the image gradients, a search is then carried out to determine if the gradient magnitude assumes a local maximum in the gradient direction. Non-maximum suppression is used to make sure $S(x,y) = 0$ if it is less than the maximum so that the width of the detected edge is one pixel. Double thresholds are used and the larger threshold is decided using the Ostu method. Once this process is complete, we have a binary image where each pixel is marked as either an edge pixel or a non-edge pixel. With the complementary output from the edge tracing step, the binary edge map obtained in this way can also be treated as a set of edge curves, which after further processing can be represented as polygons in the image domain.

The Canny edge detection method has two disadvantages. A Gaussian filter is used to smooth the image, and the scheme has a high location precision but weak smoothness and noise restraint ability with a smaller σ, such as $\sigma = 0.3$. However, with a larger σ, $\sigma = 2$ for example, the filter size increases, which will increase computation and cause serious edge shifting. On the other hand, the use of non-maximum suppression affects the accuracy of edge detection, which causes the disconnection of the edge points.

We detected tire foreign bodies and bubble defects in the tire radiography image in three sequential steps in the proposed scheme: (1) test image decomposition using total variation, (2) curvelet-based edge enhancement, and (3) an improved Canny edge detection.

To perform the total variation decomposition, we apply two low-pass filters to the gradient image by a discrete convolution. The gradient is computed by the centered difference scheme. The low pass filtered image $L_\sigma * f$ is obtained by convolving f with the low pass filter,

$$L_\sigma = (Id - (Id - G_\sigma)^n), \qquad (11)$$

where n represents that the convolution is iterated n times. We fix $n = 5$ and compute the convolutions in space under mirror boundary conditions, that is, the image is symmetrized out of its domain. In the current implementation, this low pass filtered image is obtained iteratively. The Euclidian norm of the image gradients of f and $L_\sigma * f$ is computed. The vertical and horizontal derivatives are computed by a centered two point scheme and the modulus of the gradient with an Euclidean norm. Convolve these modules

with the Gaussian G_σ to get the local total variation of f and $L_\sigma * f$. Convolutions are computed in space under mirror boundary conditions. Then we deduce the value of $\lambda(x)$ at each point in the image and the value of the cartoon image as a weighted average of f and $L_\sigma * f$. Finally, compute the texture as the difference $u(x,y) - f(x,y)$.

We can use the curvelet transform to enhance the image edges before further edge detection operations. This can be achieved by modifying the curvelet coefficients, which are modified by a function that gives rise to the drawback amplifying the noise (linearly) as well as the signal of interest. We introduce explicitly the noise standard deviation σ in the equation. The coefficients are multiplied by y_c, where y_c is defined as follows:[15]

$$y_c(x,\sigma) = 1, \text{ if } x < c\sigma,$$
$$y_c(x,\sigma) = \frac{x - c\sigma}{c\sigma}\left(\frac{m}{c\sigma}\right)^p + \frac{2c\sigma - x}{c\sigma}, \text{ if } c\sigma < x < 2c\sigma,$$
$$y_c(x,\sigma) = \left(\frac{m}{x}\right)^p, \text{ if } 2c\sigma \le x < m,$$
$$y_c(x,\sigma) = \left(\frac{m}{x}\right)^s, \text{ if } x \ge m. \qquad (12)$$

Here, the degree of nonlinearity is determined by p and the dynamic range compression is introduced by s. Using a nonzero s will enhance the faintest edges and soften the strongest edges at the same time. As is known, c becomes a normalization parameter, and a c value larger than 3 guarantees that the noise will not be amplified. The m parameter is the value under which coefficients are amplified. This value depends obviously on the pixel values inside the curvelet scale. Therefore, it is necessary to derive the m value from the data. Two options are possible:[15] (i) m can be derived from the noise standard deviation ($m = K_m\sigma$) using an additional parameter K_m. The advantage is that K_m is now independent of the curvelet coefficient values, and therefore much easier for a user to set; (ii) m can also be derived from the maximum curvelet coefficient M_c of the relative band ($m = lM_c$, with $l < 1$). In the latter case, choosing for instance $c = 3$ and $l = 0.5$, we amplify all coefficients with an absolute value between 3σ and half the maximum absolute value of the band.

When the coefficients are amplified, we reconstruct the enhanced image from the modified curvelet coefficients. We first sort the coefficients for the higher frequency bands and then select, for the magnitude, the top 1% in our experiment to reconstruct the image. Moreover, the bilateral filtering method can be used to effectively smooth the image while preserving the edges.[16,17]

For the third part of the scheme, the gradient of the cartoon part u is computed and then eight-neighborhood bilinear interpolation non-maximum suppression is applied to suppress the false edges. The

thresholding with hysteresis uses a hysteresis loop to provide a more connected result. Any pixel above the upper threshold is turned white, and the surrounding pixels are then searched recursively. If the values are greater than the lower threshold, they are also turned white. The result is that there are many fewer specks of white in the resulting image.

In performing the improved non-maximum suppression method, we divide the pixel's eight neighborhoods into four quadrants according to its gradient angle $\theta(i,j)$ with $-90° \leq \theta(i,j) \leq 90°$ and get a verdict if the pixel's gradient value is maximum or not along the direction of the pixel's gradient according to the interpolation result.[3] That is to say, when $-90° \leq \theta(i,j) \leq 0°$, we utilize the pixel's neighborhoods in the second and fourth quadrants to perform bilinear interpolation in both the horizontal and vertical directions for comparison. Otherwise, when $0° \leq \theta(i,j) \leq 90°$, we utilize the pixel's neighborhoods in the first and third quadrants to perform bilinear interpolation in both the horizontal and vertical directions.
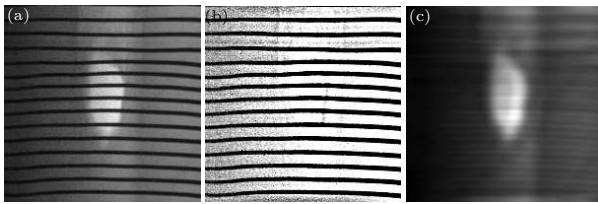

Fig. 2. The decomposition result of the tire radiography image. Left: test image, middle: texture part, right: cartoon part.

The horizontal interpolation and the vertical direction bilinear interpolation of the pixel increases the edge locating precision in our improved non-maximum suppression method. Finally, double thresholds are used and the larger threshold is decided using the Ostu method. The edge link algorithm can be used to link some of the sporadic isolated edge points together.

We provide a thorough experimental evaluation of the proposed total variation-based methodologies in the radioscopic images of tires for the detection of defects. Four typical test images that contain foreign bodies or air bubbles are selected in our tire radiography image test set. We firstly decompose the test images with Buades's fast cartoon plus the algorithm of the texture image filters. We can observe in Fig. 2 that the tire sidewall radiography image with air bubble (Fig. 2(a)) is decomposed successfully to the texture part (Fig. 2(b)) and cartoon part (Fig. 2(c)).

The contrast between the air bubbles and the background is usually not sharp enough for segmentation, which worsens the detection rate when conventional methods are used. On the other hand, the variety in their shapes and the uneven background make the detection even more difficult. As can be seen

in Fig. 2, the total variation based image decomposition methodologies perfectly decompose the test image into the texture part and cartoon part, which therefore makes defect detection feasible using conventional methods. As a matter of fact, even when lowering the contrast between the air bubble and background, the decomposition result is perfect, so the bubble and texture information is segmented completely in a near lossless way.
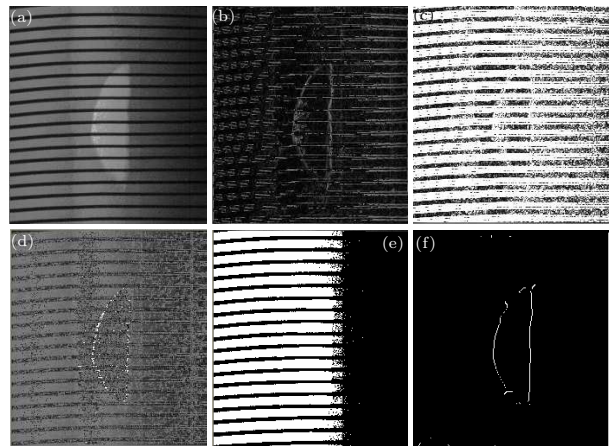
Fig. 3. Experimental results of the detection of tire foreign bodies and bubble defects using conventional methods. (a) Tire bubble defect test image, (b) Sobel edge detection result, (c) LoG edge detection result, (d) watershed method result, (e) image adaptive thresholding results, and (f) the result of the proposed method.
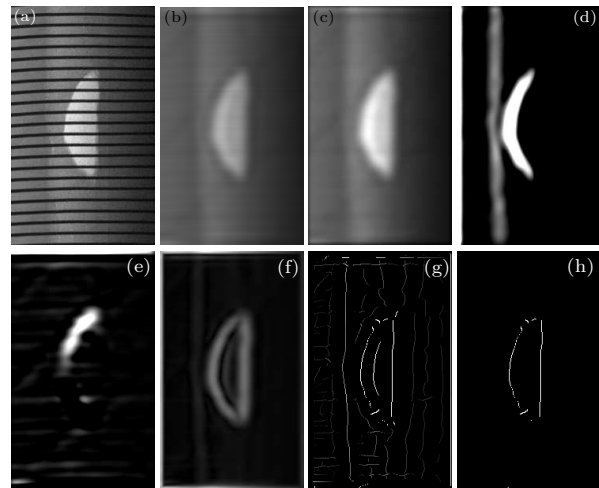
Fig. 4. The experimental result of the tire radiography image defect detection using the improved Canny edge detection method on the cartoon part of the image. (a) Test image; (b) the cartoon part decomposed from the test image; (c) filtered (b) with a Gaussian filter (with $\sigma = 4$); (d) the x gradient of (c); (e) the y gradient of (c); (f) the gradient magnitude of (c); (g) locating at the edges with non-maximal suppression, and (h) thresholding (g) to eliminate spurious responses.

In our experiments, the Sobel operator, the LoG operator and Canny edge detection algorithms, the watershed method and the adaptive thresholding method are employed for comparison. Figure 3 shows

the experimental results of tire foreign bodies and bubble defect detection using conventional methods. The air bubble region values of the pixels in the tire radiography images are relatively larger than that of the background; however, the contrast between them is not sharp enough (see Fig. 3(a)) to be detected using conventional edge detection algorithms directly, as can be seen in Figs. 3(b) and 3(c). We also perform the experiment on the tire bubble defect image using the watershed method. However, the over-segmentation problem will ruin the detection result since the watershed method is sensitive to the uneven irradiation background that is usually seen in tire radiography images, see Fig. 3(d). The uneven irradiation distribution is random because of the variation in the tire thickness and other parameters, and thus it cannot be revised by gray level correction techniques. Moreover, the gray levels of the tire bubble regions and the background vary because of their different locations in the tire, which will yield a multi-peak histogram. Therefore, the adaptive thresholding method will not be an efficient method for the whole test image, see Fig. 3(e). Figure 3(f) gives the experimental result using our proposed method.

Figure 4 shows the detection result of a tire sidewall radiography image with bubble defect. After total variation based image decomposition, the cartoon part is enhanced and filtered with a Gaussian filter (with $\sigma = 4$) to denoise; see Fig. 4(c). The gradient is then computed, as can be seen in Figs. 4(d), 4(e) and 4(f), respectively. Non-maximal suppression is used to locate the edges (see Fig. 4(g)) and double thresholding is used to eliminate spurious responses (see Fig. 4(h)). Here, we set the double thresholds T_1 and T_2 as $T_1 = 0.1$ and $T_2 = 0.3$, respectively. It can be seen in Fig. 4(h) that the tire defect in the test radiography image is detected and located perfectly. There are spurious edges in Fig. 4(h) even after thresholding. However, these edge contours are usually harmless, and even if they are not removed by thresholding, they will be discarded by our subsequent algorithm since they contain no major edges. On the other hand, the edge is not continuous as expected, and thus a continuous edge operation is needed in a further process.

Figure 5 shows the experimental results on tire radiography images with various defects, such as a foreign object and line-art bubble defect. The presented method also achieves satisfying performances on different patterns of defect. The edges of the defects are detected and located successfully, and the false edges are eliminated at the same time, except that the edge is not as clear-cut as that of Fig. 4 since the bubble edge of Fig. 5(a) is not as sharp as that of Fig. 4(a).

In Fig. 5(c), the line-art bubble is relatively long and thin. Moreover, the background near the de-

fect has a higher gray level. However, as is shown in Fig. 5(f), the detection result reflects the characteristics of the defect that need to be detected relevantly.
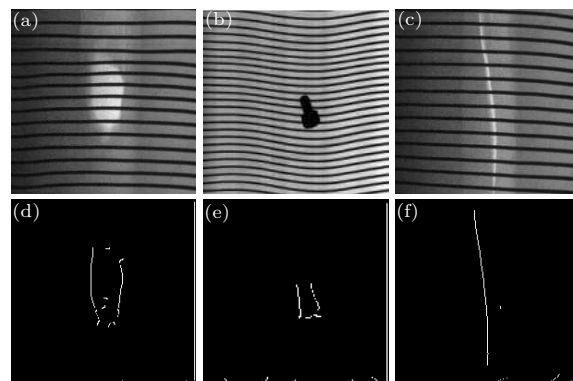
Fig. 5. Experimental results on tire radiography images with different defects using the proposed detection method on the cartoon part images. Upper: test images; lower: detection results.

Even though we can locate the defect through the detection results, we probably cannot measure the width and length of the defect. This is because the gradient of the defect becomes inconspicuous at both ends. We could regulate the parameters to obtain the real length, however, this would produce fake edges of the background with a higher gray level.

In summary, we have investigated the detection of foreign bodies and bubble defects in tire radiography images based on total variation image decomposition, curvelet image enhancement and edge detection in three sequential steps. The scheme is efficient to implement and can be applied to similar problems. The experimental results indicate that foreign bodies and bubbles in tires can be detected and located accurately.

References

[1] Ioannis V and Dimitrios K 2010 *Expert Syst. Appl.* **37** 7606
[2] Anouncia S M and Saravanan R 2006 *Insight Non-Destr. Test. Cond. Monit.* **48** 592
[3] Zhang Y et al 2013 *Opt. Laser Technol.* **47** 64
[4] Ding D H et al 2004 *Chin. Phys. Lett.* **21** 1067
[5] Mery D and Filbert D 2002 *IEEE Trans. Rob. Autom.* **18** 890
[6] Fillatre L et al 2007 *J. Comput.* **2** 26
[7] Bo W R G et al 2003 *Chin. Phys.* B **12** 610
[8] Di Q Y et al 2009 *Acta Phys. Sin.* **58** 9 (in Chinese)
[9] Nacereddine N et al 2006 *Proc. ECNDT* **2** 4
[10] Sofia M and Redouane D 2002 *Proc. ECNDT*(Barcelona) p 17
[11] Carrasco M A and Mery D 2004 *Mater. Eval.* **62** 1142
[12] Buades A et al 2010 *IEEE Trans. Image Process.* **19** 1978
[13] Luminita A V and Stanley J O 2003 *J. Sci. Comput.* **19** 553
[14] Shapiro L G and Stockman G C 2001 *Computer Vision* (London Prentice Hall) p 326
[15] Starck J et al 2003 *IEEE Trans. Image Process.* **12** 706
[16] Li J C et al 2012 *Acta Phys. Sin.* **61** 189501 (in Chinese)
[17] Li J C et al 2012 *Acta Phys. Sin.* **61** 119501 (in Chinese)